

Journal of Electronic Imaging

SPIEDigitalLibrary.org/jei

Image segmentation with adaptive region growing based on a polynomial surface model

Francis Deboeverie
Peter Veelaert
Wilfried Philips



Image segmentation with adaptive region growing based on a polynomial surface model

Francis Deboeverie

Peter Veelaert

Wilfried Philips

Ghent University

Image Processing and Interpretation/iMinds

St-Pietersnieuwstraat 41

B9000 Ghent, Belgium

E-mail: Francis.Deboeverie@telin.ugent.be

Abstract. A new method for segmenting intensity images into smooth surface segments is presented. The main idea is to divide the image into flat, planar, convex, concave, and saddle patches that coincide as well as possible with meaningful object features in the image. Therefore, we propose an adaptive region growing algorithm based on low-degree polynomial fitting. The algorithm uses a new adaptive thresholding technique with the L_∞ fitting cost as a segmentation criterion. The polynomial degree and the fitting error are automatically adapted during the region growing process. The main contribution is that the algorithm detects outliers and edges, distinguishes between strong and smooth intensity transitions and finds surface segments that are bent in a certain way. As a result, the surface segments corresponding to meaningful object features and the contours separating the surface segments coincide with real-image object edges. Moreover, the curvature-based surface shape information facilitates many tasks in image analysis, such as object recognition performed on the polynomial representation. The polynomial representation provides good image approximation while preserving all the necessary details of the objects in the reconstructed images. The method outperforms existing techniques when segmenting images of objects with diffuse reflecting surfaces. © 2013 SPIE and IS&T [DOI: 10.1117/1.JEI.22.4.043004]

1 Introduction

Image segmentation is an important primary step in many computer vision applications, for instance, object recognition. Ideally, an image segmentation algorithm divides an image into separate regions, which correspond to different object features or areas of interest.¹ For instance, in a face image, meaningful object features are the lips, the eyebrows, etc. Then, an accurate classification of image segments is the next step to perform object recognition. In this work, segmentation divides gray-scale images into surface segments (intensity patches) with adaptive region growing based on low-degree polynomial fitting. The main novelty is that the algorithm removes outliers, stops at real-image object edges, distinguishes between strong and smooth intensity transitions, and considers the segment curvature, such as flatness, convexity, or concavity. The outliers are gray values differing from their neighbors due to noise or small object

speckles in the image. As a result, the adaptive region growing finds smooth surface segments of maximal size, such that image intensities can be approximated sufficiently well by a low-degree polynomial function (e.g., 0, 1, or 2). The curvatures of these polynomials roughly classify object features into flat, planar, convex, concave, and saddle patches. This approach is based on the property that, because of Lambert's cosine law,² when the light comes mainly from one direction, the intensity surface of an image has the same shape as the object surface itself. For instance, human skin is such a diffusely reflecting surface. Then, a face, which resembles a convex sphere with small concavities, will be seen as a collection of intensity patches of concave functions and smaller patches of convex functions.³ This curvature-based surface shape classification delivers relevant information to perform image analysis, such as an object recognition performed on the polynomial representation.

1.1 Related Works

Over the past few decades, the image segmentation has been studied extensively with a huge number of algorithms being published in the literature.^{4–8} The image segmentation approaches are often divided broadly into three categories: feature-based,^{9–16} region-based,^{17–22} and graph-based.^{23–25} The feature-based image segmentation collects the main characteristics of an image by extracting image features, which are usually based on the color or texture. The feature samples are handled as vectors. The objective is to group the extracted feature vectors into well-separated clusters by using a specific distance metric. Drawbacks of these methods are the nonpreservation of spatial structure and edge information and the possible grouping of pixels from disconnected regions of the image with overlapping feature spaces. In the spatial domain, region-based image segmentation preserves the edge information and the spatial relationship between pixels in an image. The objective is to detect regions that satisfy predefined criteria in a region-growing, region-merging or region-splitting process. The graph-based image segmentation fuses the feature-based and region-based information. Grouping is based on several important elements, such as similarity, proximity, and continuation. A weighted graph can be constructed, where each vertex corresponds to a pixel or region, and the associated weight of

Paper 13060 received Feb. 5, 2013; revised manuscript received Aug. 27, 2013; accepted for publication Sep. 9, 2013; published online Oct. 2, 2013.

0091-3286/2013/\$25.00 © 2013 SPIE and IS&T

each edge connecting two adjacent pixels or regions depends on the likelihood that they belong to the same region. The weights are often related to color and texture features. Given the above-mentioned three segmentation categories, in this study, we consider the spatial-based image segmentation in a region-growing process based on a polynomial fitting criterion.

The segmentation of intensity images with polynomial fitting is originating from segmented image coding (SIC).^{26–33} The main idea of SIC is to divide the image into segments that coincide as well as possible with meaningful parts in the image. Each region is represented by two codes. The first (often a chain code) describes the location of contour pixels. The second represents the best approximation of the region enclosed by this boundary. For these techniques, the main purpose was image compression. With respect to SIC, this paper deals with the segmentation of gray values into image regions and not with coding techniques. The above-mentioned techniques subdivide large regions artificially because low-degree polynomials cannot represent large regions accurately. However, contours separating artificial regions do not correspond to real-image object edges. This is detrimental to our objective of using polynomial surface segments for image analysis. In this work, due to smart treatment of outliers and edges, the surface segments correspond to object features and the contours separating the surface segments coincide with real-image object edges. Another difference is that many of these methods are stated as least squares or L_2 norm³⁴ optimizations. In contrast, we examine the approach based on the L_∞ norm,³⁴ which allows us to easily make decisions during region growing about adding a new pixel, discarding an outlier or stopping at an edge. Also, we propose algorithms with linear time complexity.

In literature, researchers have, mainly, been investigating surface segmentation in range images.^{35–38} One popular approach for surface segmentation is region growing, for which several segmentation criteria have been proposed. A distinction is made between segmentation based on normal vectors,^{39,40} curvatures,^{41–45} and fitting polynomials.^{46–48} Existing techniques using low-degree polynomial fitting for surface segmentation consider planar patches⁴⁸ and quadratic patches,^{49–51} such as circular cylinders⁵² and ellipsoidal surfaces.⁵³ These techniques are often not suited to segment intensity images. This is caused by the different behavior of range images and intensity images. Range images are often smooth and represent the real object while gray values in intensity images are more textured because they represent reflected light. Therefore, segmenting intensity images with region growing^{54–56} requires an adaptive approach, which can handle the local and global variation of gray values.^{57,58}

1.2 Contributions

In this work, we propose a novel intelligent technique to segment gray-scale images into smooth surface segments with adaptive region growing. Therefore, we present a criterion for region growing which is based on constructive polynomial surface fitting.^{59,60} Constructive fitting aims to minimize the L_∞ fitting cost. In the past, the L_∞ norm was already used to remove outliers as a first step before L_∞ optimization.⁶¹ Here, we propose an adaptive thresholding of the L_∞ fitting cost as a stopping criterion and to distinguish outliers and edges from gently rising variation. The adaptive

thresholding allows for a variable polynomial degree and a variable fitting error, depending on the local image properties. This work on surface segmentation is a multivariate extension of our work on the adaptive thresholding for contour segmentation.⁶² The novelty is that the region growing investigates the local variation of gray values in a segment to identify edges and outliers, whereas the global variation of gray values in a segment is investigated to adapt the degree of the polynomial surface. The combination of both is possible because we employ constructive fitting: the global fitting cost is calculated from local fitting costs. The following list gives an overview of the properties of our algorithm, which are essential for robust segmentation of smooth surfaces:

- The algorithm identifies and discards outliers.
- The region growing stops at real-image edges.
- The low-degree surface fitting allows for smooth variations of the image intensities.
- The algorithm classifies segments into flat, planar, convex, concave, and saddle surfaces.
- The algorithm's processing speed does not depend on segment size.
- The region growing stops when the variation of gray values becomes too large to capture it with a single low-degree polynomial surface.

We evaluate the proposed segmentation method on the Berkeley segmentation dataset and benchmark (BSDS300).⁶³ To measure the difference between two segmentations, we examine the probabilistic rand index (PRI).⁶⁴ In literature, there is an abundance of segmentation results on the BSDS300. A few recent results can be found in Refs. 65–68. As we will show, when segmenting images of objects with diffuse reflecting surfaces, our method outperforms existing segmentation techniques, such as normalized cuts,²³ mean shift,¹² and power watersheds.²⁵ Furthermore, we gain additional information of the shape of the objects in the images with curvature-based shape analysis.

The remainder of this paper is organized as follows. Section 2 describes the new segmentation algorithm, which is an adaptive region growing algorithm based on low-degree polynomial surface fitting. We treat all possible problems that arise in the segmentation of an image surface with region growing. Section 3 describes how to classify segments based on the curvatures of the approximating polynomial surfaces. Section 4 presents the results of the proposed segmentation technique.

2 Segmentation with Adaptive Region Growing

This section describes the algorithm to segment a gray-scale image into smooth surface segments with adaptive region growing based on low-degree polynomial fitting. We explain how the region growing is made adaptive to the local image properties, such that patches are represented as polynomial surfaces with a variable polynomial degree and a variable fitting error.

2.1 Constructive Polynomial Surface Fitting

In this work, we find regions of maximal size that satisfy an L_∞ fitting cost criterion, such that image intensities can be approximated sufficiently well by a low-degree polynomial

function. Let $f(x_i, y_i)$ represent the image intensities. Let G be a vector space of fitting functions, for instance, the vector space of bivariate polynomial functions of degree d :

$$g(x, y) = \sum_{k=0}^d \sum_{l=0}^k \alpha_{l,k-l} x^l y^{k-l}, \quad (1)$$

where each polynomial is characterized by $n = (d+1)(d+2)/2$ coefficients $\alpha_{l,k-l}$.

The accuracy of fitting $g(x, y)$ over the segment S is measured with the L_∞ fitting cost. This fitting cost is defined as

$$r(S; g) = \max_{(x,y) \in S} |g(x, y) - f(x, y)|. \quad (2)$$

The best fit is the polynomial function $g(x, y)$ in G for which $r(S; g)$ is minimal. We denote this minimal cost as $r(S)$, i.e.,

$$r(S) = \min_{g \in G} r(S; g). \quad (3)$$

The L_∞ fitting cost over any segment S can be estimated very efficiently in terms of so-called elemental subsets.^{59,60} These are subsets of S that contain precisely m points. Introducing elemental subsets will bring the advantage of minimizing the time to compute the fittings costs when adding new pixels to large segments during a region growing process, as explained in the following section. The importance of an elemental subset lies in the fact that the fitting cost over an elemental subset can be computed in a straightforward manner. Let $D = \{(x_1, y_1), \dots, (x_m, y_m)\}$ be an elemental subset. Let E_j denote the cofactor (signed minor) of the element at the intersection of the last column and the j 'th row of the following matrix:^{59,60}

$$(A_D | B_D) = \begin{pmatrix} 1 & x_1 & y_1 & x_1^2 & x_1 y_1 & y_1^2 & \cdots & f(x_1, y_1) \\ \vdots & \vdots & \vdots & \vdots & \vdots & \vdots & \ddots & \vdots \\ 1 & x_m & y_m & x_m^2 & x_m y_m & y_m^2 & \cdots & f(x_m, y_m) \end{pmatrix}. \quad (4)$$

Then one can show that the fitting cost over an elemental subset D can be computed by

$$r(D) = \frac{\det(A_D | B_D)}{|E_1| + \dots + |E_m|} = \frac{|E_1 f(x_1, y_1) + \dots + E_m f(x_m, y_m)|}{|E_1| + \dots + |E_m|}, \quad (5)$$

provided the denominator is nonvanishing.^{59,60} If the denominator is vanishing, $r(D)$ is discarded. Furthermore, the fitting cost over any segment S that contains more than m points is

$$r(S) = \max_{D \in U} r(D), \quad (6)$$

where U is the collection of all elemental subsets D of S for which $|E_1| + \dots + |E_m| > 0$. Equation (6) holds when U is nonempty, which is the case as soon as not all the points of the segment lie exactly on a common curve, $g(x, y) = 0$.

Figure 2(a) shows an example of the points of an elemental subset (gray squares) of a segment S (gray and white squares). In this example, the fitting costs are computed for polynomial functions of degree $d = 2$. Consequently, the number of points in the elemental subset is $m = 7$.

In principle, to find $r(S)$, we must evaluate $r(D)$ over all possible elemental subsets of S , a collection that grows as $O(|S|^m)$ when the segment grows larger. However, we can obtain a reliable estimate of the fitting cost with far fewer computations than those required for computing the fitting cost exactly. The fitting cost of a dataset can be estimated very reliably from a few of its elemental subsets.^{59,60} Instead of calculating $r(S)$, we compute the estimate

$$\tilde{r}(S) = \max_{D \in \tilde{W}} r(D), \quad (7)$$

where \tilde{W} forms a rigid subcollection of M elemental subsets of S .^{59,60} To be rigid, it is necessary that each pixel is covered by at least one elemental subset and that each elemental subset, which has m points, has at least $m - 1$ points in common with all of the other sets. In a region-growing process, these conditions are met automatically. In the experiments, we achieve reliable estimation of the fitting cost by randomly selecting a small fixed number (e.g., $M = 10$) of elemental subsets D . Decreasing the number of elemental subsets will decrease the computation time. However, the fitting cost will be estimated less accurately.

During region growing, the L_∞ fitting cost shows direct response to intensity discontinuities since the L_∞ norm looks at the maximum deviation between pixel values and the fitting polynomial. This is advantageous in region growing when making decisions about adding a new pixel, discarding an outlier, or stopping at an edge. For each pixel to be added in region growing, the fitting cost in Eq. (7) is computed when fitting a polynomial surface to the pixel and the segment. The fitting cost is an indicator of whether the pixel belongs to the segment according to the polynomial. It is computed without computing the actual best fitting polynomial. The best fit has only to be computed when the segment is finished. The best L_∞ fit is computed in $|S| \log |S|$ time and gives the precise value of the error.⁶⁹

2.2 Adaptive Region Growing with Elemental Subsets

Computing the fitting cost with elemental subsets boils down to a sampling of the image region. Sampling allows us to find out how each pixel in an image region contributes to the fitting cost when fitting a polynomial to that region. Fitting costs can be computed for local regions as well as for a global region, where the corresponding global fitting cost is calculated from the corresponding local fitting costs. Moreover, the local and global fitting costs can be combined in several ways. For example, in Fig. 1(a), we compute the local fitting cost when fitting a polynomial to the pixels of the regions S_1 and S_2 . At the same time, this local fitting cost is a part of the global fitting cost when fitting a polynomial to the pixels of the regions S_3 and S_4 . In fact, for the estimated fitting cost, we have $\tilde{r}(S_4) = \max\{\max_{D \in \tilde{W}_4} r(D), \max_{D \in \tilde{W}_3} r(D), \max_{D \in \tilde{W}_2} r(D), \max_{D \in \tilde{W}_1} r(D)\}$, where $S_1 \subset S_2 \subset S_3 \subset S_4$.

In this paper, we demonstrate the key idea of combining local and global fitting costs with a strategy for image

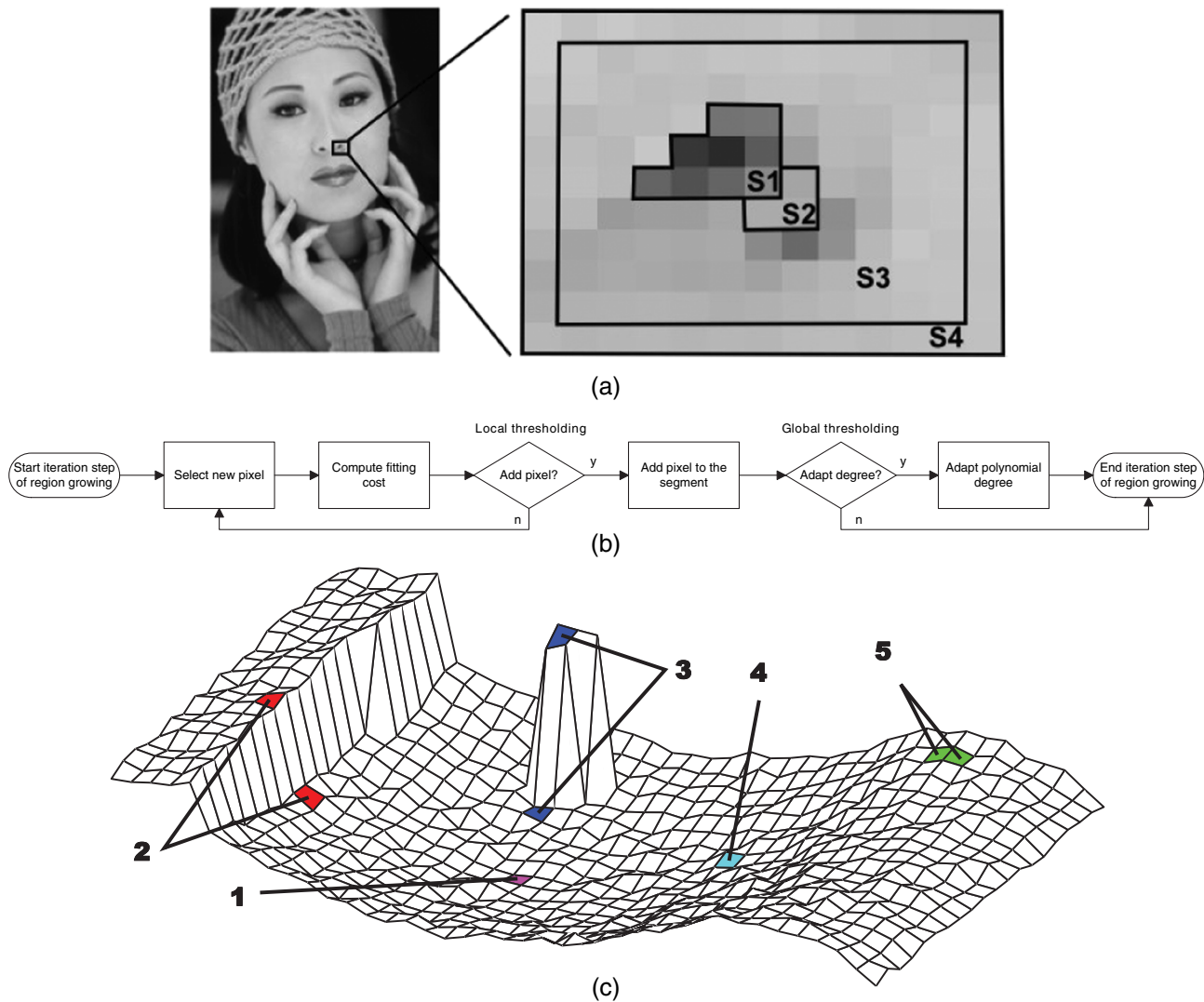


Fig. 1 Adaptive region growing: (a) Computing the fitting cost with elemental subsets allows discovery of how each pixel in an image region contributes to the fitting cost when fitting a polynomial. In this example, we compute the local fitting cost when fitting a polynomial to the pixels of the regions S_1 and S_2 . At the same time, this local fitting cost is a part of the global fitting cost when fitting a polynomial to the pixels of the regions S_3 and S_4 . (b) Flow chart of one iteration step in the adaptive region growing. Two key phases are distinguished: the first determines if a new pixel is to be added to a segment, whereas the second phase controls if the polynomial degree is adapted. (c) An example of image intensities which we segment into smooth surface segments with adaptive region growing and polynomial fitting. Case 1: Seed pixels are chosen as local extrema of the image. Case 2: The region growing stops at edges. Case 3: The algorithm grows around outliers. Edge pixels and outliers are not added to the segment because that would cause too fast and too direct increases in the L_∞ fitting cost. Case 4: The polynomial degree is adapted when the variation of gray values is smooth but too large to capture it with the current polynomial degree. Case 5: The segmentation starts with a new segment when the variation of gray values becomes too large to capture it with a flat, planar, convex, concave, or saddle like surface.

segmentation in a region-growing process with adaptive thresholding. The proposed region-growing method examines the thresholding of local fitting costs to decide if a new pixel is to be added to a segment (to identify edges and outliers), whereas the thresholding of global fitting costs controls whether or not the polynomial degree is adapted. We distinguish two key phases in our region-growing strategy, which is visualized in the flowchart in Fig. 1(b). The first phase determines if a new pixel is to be added to a segment. The second phase controls whether or not the polynomial degree is adapted. These phases are driven by the adaptive thresholding of the L_∞ fitting cost $\tilde{r}(S)$. This will become clear when we explain the region-growing based on the segmentation of the image surface in Fig. 1(c). Segmenting this image surface covers all the possible

problems we have to deal with in region growing. Five cases are considered.

2.2.1 Case 1: Start region growing

The region growing starts with a seed pixel and then repeatedly adds new pixels to the segment as long as the segmentation criterion is still satisfied on the enlarged segment. Seed pixels are automatically chosen as local gray value extrema of the image and where the gradient remains small. This avoids the selection of seed pixels at an edge since seed pixels at an edge offer fewer opportunities to grow. In the experiments, we achieve optimal segmentation results for seed pixels chosen as gray value extrema in a neighbor size of 3% of the image area (e.g., a 34×34 neighborhood for

images of size 240×160). For each new seed pixel, we start with the polynomial degree set equal to zero in Eq. (1). Case 1 in Fig. 1(c) shows an example of such a seed pixel. Pixels are then added one by one. Pixels to be added are selected from pixels next to the boundaries of the segment.

2.2.2 Cases 2 and 3: Stop at edge pixels and grow around outliers

For each pixel p_i already added to the segment S_i , the region growing keeps track of the fitting cost when fitting a low-degree polynomial surface to S_i and p_i . To this end, we define

$$\tilde{r}(S_i; p_i)$$

as the cost of adding p_i to S_i .

The decision to add a new pixel p_k , for which we introduce a local neighborhood R_k , is then based on

$$X_k = \tilde{r}(S_k; p_k) - \frac{1}{|R_k|} \sum_{p_i \in R_k} \tilde{r}(S_i; p_i) \leq T_X, \quad (8)$$

which measures the local behavior of the fitting costs. A segment will grow until the local variation of the gray values

changes, giving rise to discontinuities in the fitting costs. However, to avoid over-reaction to discontinuities due to noise and small speckles, the increase in fitting cost is compared to the mean of previous fitting costs in the local neighborhood R_k of p_k . Figure 2(b) shows an example of p_k (black square) and R_k (gray squares) in S_k (white and gray squares). The new pixel p_k is added to S_k when X_k is lower than the threshold T_X . When X_k exceeds T_X , i.e., when adding p_k would increase the fitting cost significantly more than on average, p_k is not added to S_k . Figure 3(a) shows a one-dimensional (1-D) example of a strong transition in the variation of data points, which causes a fast and direct increase in the L_∞ fitting costs. This occurs when p_k is an outlier or lies on an edge. If p_k is an outlier, the segment will grow around p_k . Cases 2 and 3 in Fig. 1(c) show examples of such an edge and outlier, respectively.

Thus, the stopping criterion during region growing depends on the local differences between the fitting costs, not on their magnitude. The discontinuities (outliers and edges) are distinguished from gently rising variation.

2.2.3 Case 4: Adapt the polynomial degree

The decision to increase the degree of the polynomial surfaces is based on

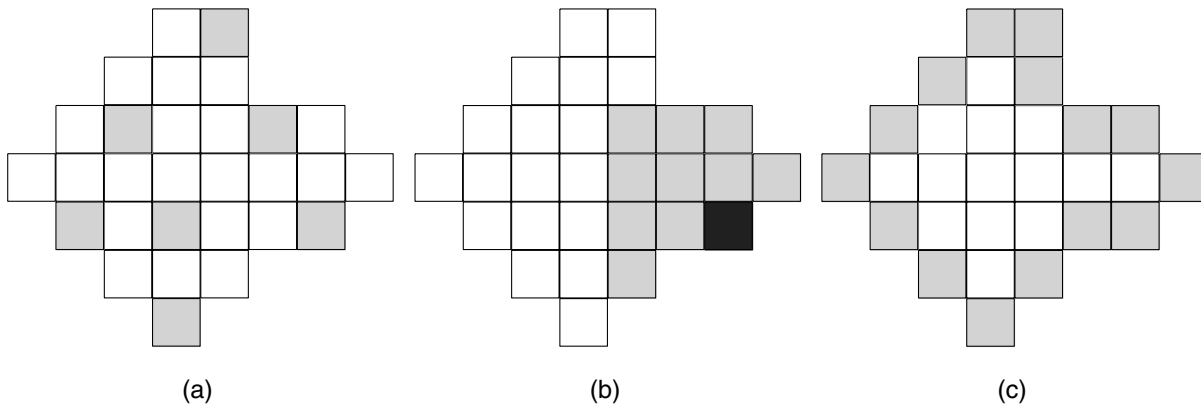


Fig. 2 Elemental subsets, adding pixels and adapting the polynomial degree: (a) An example of the points of an elemental subset (gray squares) of a segment S (gray and white squares). (b) An example of a new pixel p_k (black square) and a local neighborhood R_k (gray squares) in the segment S_k (white and gray squares), which determine whether to add the black pixel to the segment. (c) An example of the pixels p_i on the boundary B_i (gray squares) in the segment S_i (white and gray squares), which determine whether to increase the polynomial degree.

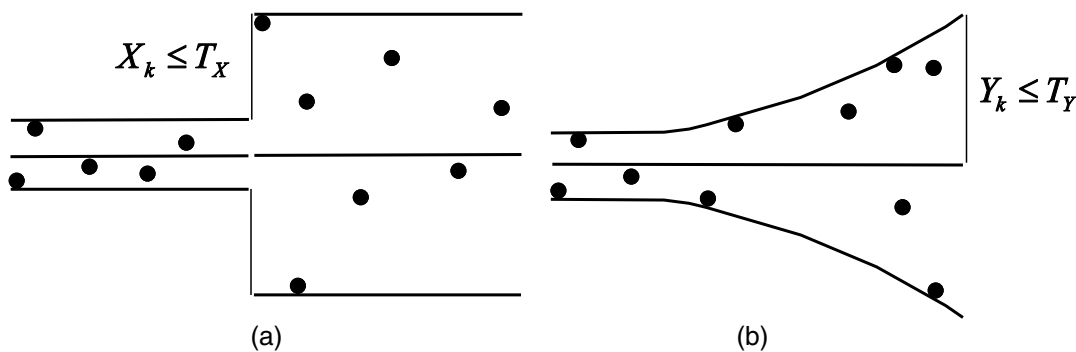


Fig. 3 One-dimensional (1-D) adaptive thresholding of the L_∞ fitting cost: (a) 1-D example of a strong transition in the variation of data points, which causes a fast and direct increase in the L_∞ fitting costs. A data point is added to the segment if X_k , which measures the local behavior of the fitting costs, is lower than the threshold T_X . (b) 1-D example of a smooth transition of data points, which causes a smooth increase in the L_∞ fitting costs. The polynomial degree is increased by one if Y_k , which measures the global behavior of the fitting costs, exceeds the threshold T_Y .

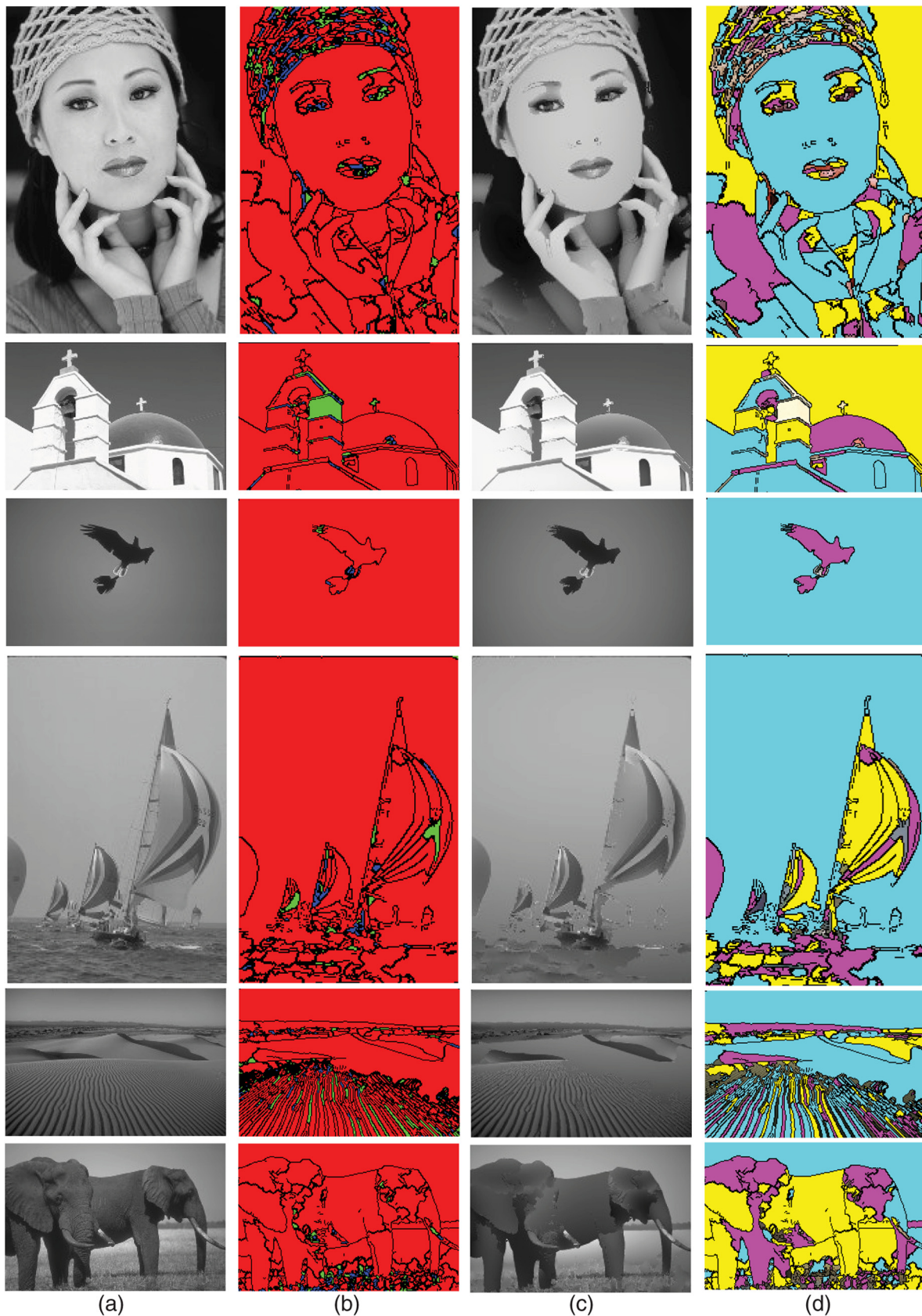


Fig. 4 Segmentation results on the BSDS300: (a) Gray-scale images with image size 240×160 . (b) The segmented images with the corresponding probabilistic rand indices (PRIs). The blue, green, and red colors in the segmented image correspond to zero, first, and second degree polynomial surfaces, respectively. Many surface segments correspond to meaningful parts of the image. (c) The surface approximated images. Objects are nicely approximated by the low-degree polynomial surfaces. (d) The convex, concave, or saddle like behavior of the second-degree polynomial surfaces, indicated in the colors magenta, cyan, and yellow, respectively. Convex object parts with diffuse reflecting surfaces are seen as intensity patches of a concave functions.

$$Y_k = \frac{1}{|B_i|} \sum_{p_i \in B_i} \tilde{r}(S_i; p_i) \leq T_Y, \quad (9)$$

which measures the global behavior of the fitting costs. It is determined by the mean of the fitting costs when fitting a low-degree polynomial surface to the segment S_i and the pixels p_i on the boundary B_i . These fitting costs contain all recent information about the maximum deviation between the pixels of S_i and the polynomial surface. B_i grows when S_i gets larger. Figure 2(c) shows an example of the pixels p_i on B_i (gray squares) in S_i (white and gray squares). The polynomial degree is increased by one when the global variation of gray values becomes too large. This is when Y_k exceeds the threshold T_Y . Then, Y_k is recomputed for this new degree. In fact, the degree increases until either Y_k is again within the limit of the threshold T_Y or a maximum degree is exceeded. In this paper, the maximal polynomial degree is two, which is sufficient to expand the segment along smooth flat, planar, convex, concave, and saddle intensity functions. Figure 3(b) shows an 1-D example of a smooth transition of data points, which causes a smooth increase in the L_∞ fitting costs. Case 4 in Fig. 1(c) shows a pixel where the variation of gray values is smooth but too large to capture it with the current polynomial degree.

Thus, the adaptation of the polynomial degree depends on the global behavior of the fitting costs. The global behavior at the boundary reveals whether a smooth segment is slowly evolving toward either a flat, planar, convex, concave, or saddle surface.

2.2.4 Case 5: Discontinuity region growing

When no more pixels can be added along the boundary, the segment is completed and the segmentation process starts a new segment in a new seed pixel. Case 5 in Fig. 1(c) shows a pixel where a new segment is created because the variation of gray values becomes too large to capture it with a single flat, planar, convex, concave, or saddle like surface.

The growing process has been designed to find smooth segments in an image. It will grow around outliers and it will stop at edges. However, there is no guarantee that two segments sharing a common boundary will stop exactly at the same edge. The treatment of this issue requires some additional processing.

To force segments to stop at the same common boundary, we do not allow the segments to grow over strong edges of an edge map. The Canny edge detector is suitable, because it results in thin edges of one pixel thickness, similar to the segment boundaries in the region growing. In addition to the edges of the edge detector, the segmentation will find additional edges at the segment boundaries, which are much smoother than the edges found by an edge detector. These additional edges are necessary in the segmentation. They represent smooth meaningful transitions in a surface, e.g., the gradual transition from a concave surface into a convex surface.

Since large segments in an image often represent important object features, at a smooth transition, a new segment A is allowed to grab pixels from an existing segment B. For this to happen, we require that A must already be larger than B and the polynomial degree of A must not be lower than the polynomial degree of B.

Finally, morphological closing is used to fill the gaps in the segments. Thus, outliers, which violate the conditions of not exceeding T_X and T_Y , but which are enclosed by a segment, are added to the segment. Similarly, we prevent the segmentation from resulting in many small segments (e.g., ≤ 10 pixels). Therefore, if possible, we add small segments to larger adjacent segments under less strong conditions.

3 Classification with Polynomial Curvatures

This section describes how to classify segments into flat, planar, convex, concave, or saddle patches based on the curvatures of the polynomial surfaces.

From the segmentation, it is known that each surface segment can be approximated by a low-degree polynomial surface as in Eq. (1). Then, the intensity function of a segment is represented by its polynomial coefficients. The coefficients are computed after all segments have been found. Remember that during region growing, only the fitting cost was computed. A method for computing the best L_∞ fit is described in Ref. 69.

Convex, concave, or saddle like behavior of a second-degree polynomial surface $g(x, y)$ as in Eq. (1) is defined by the signs of the eigenvalues of the Hessian matrix:

$$H(g) = \begin{bmatrix} \frac{\partial^2 g}{\partial x^2} & \frac{\partial^2 g}{\partial x \partial y} \\ \frac{\partial^2 g}{\partial x \partial y} & \frac{\partial^2 g}{\partial y^2} \end{bmatrix}. \quad (10)$$

The entries of the matrix $H(g)$ are second derivatives of the surface with respect to x and y coordinates. For a quadratic surface, the second derivatives are constant and hence, $H(g)$ is independent of location. From Eq. (1)

$$H(g) = \begin{bmatrix} 2\alpha_{2,0} & \alpha_{1,1} \\ \alpha_{1,1} & 2\alpha_{0,2} \end{bmatrix}. \quad (11)$$

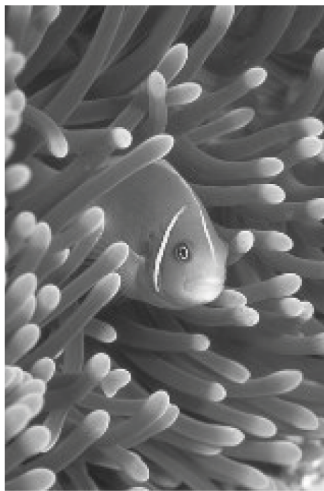
The maximum and minimum curvatures are given by the eigenvalues of this matrix, which are found by solving the following characteristic equation:

$$Hk = \lambda k. \quad (12)$$

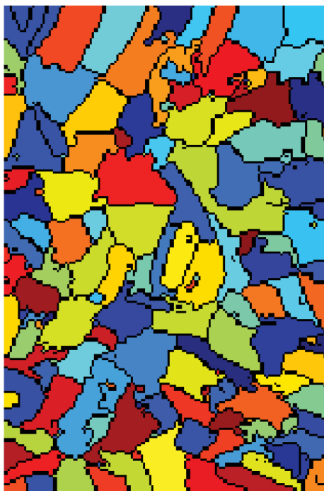
Since H is a 2×2 matrix, its eigenvalues are found by solving the following quadratic equation:

Table 1 Performance statistics on the BSDS300.

BSDS300	Performance statistics
Image size	240 × 160
Computation time (ms)	1156 ± 185
Mean fitting cost	2.51 ± 0.93
#Surfaces	35.52 ± 8.91
PRI	0.74 ± 0.16



(a)



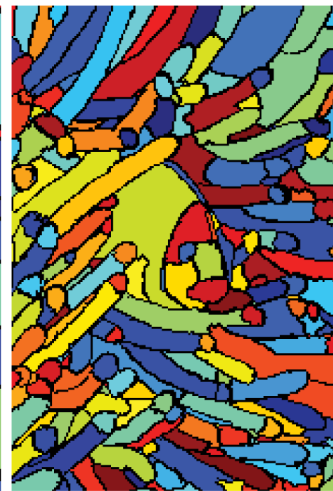
(b)



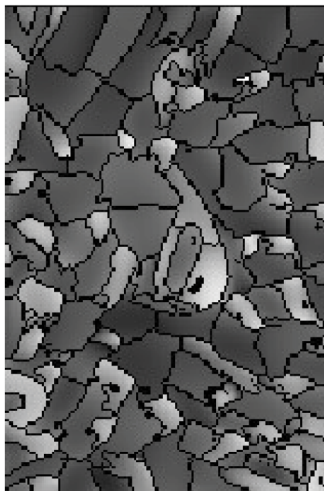
(c)



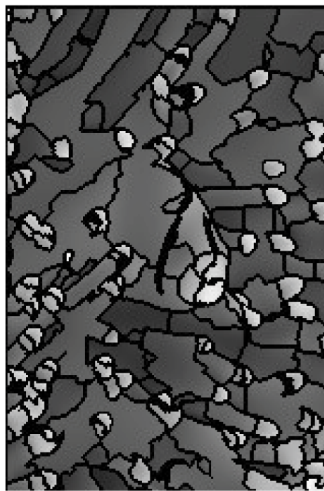
(d)



(e)



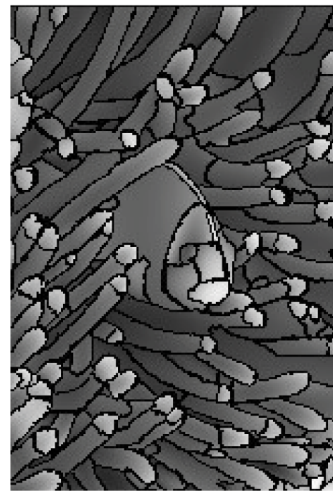
(f)



(g)



(h)



(i)

Fig. 5 Visual comparison between segmentation techniques: columns (b)–(e) on the second row show segmentations of the fish image with diffuse reflecting surfaces in (a), produced by normalized cuts (Ref. 23), mean shift (Ref. 12), power watersheds (Ref. 25) and polynomial surfaces, respectively. For these segmentation techniques, columns (f)–(i) on the third row show the segment approximations with polynomial surfaces of second degree as in Eq. (1). In contrast to existing segmentation techniques, the segments produced by the proposed method correspond more to object features, the contours separating the surface segments coincide with real-image object edges and the low-degree polynomial approximations accurately reconstruct the image.

Table 2 Probabilistic rand index (PRI) results on the BSDS300.

PRI (higher is better)	BSDS300	Subset 1	Subset 2
Human	0.87	0.83	0.90
Polynomial surfaces	0.74	0.67	0.84
Power watersheds	0.77	0.74	0.79
Mean shift	0.76	0.72	0.77
Normalized cuts	0.72	0.69	0.74

$$\begin{vmatrix} 2\alpha_{2,0} - \lambda & \alpha_{1,1} \\ \alpha_{1,1} & 2\alpha_{0,2} - \lambda \end{vmatrix} = 0. \quad (13)$$

The matrix H is symmetric, hence the solution yields two real values λ_1 and λ_2 . Both λ_1 and λ_2 are positive for a convex surface and negative for a concave surface. Eigenvalues have opposite signs for a saddle surface.

In the following section, we show that the determination of the curvatures of polynomial surfaces is an effective method for segment classification. We classify segments into flat, planar, convex, concave, or saddle patches. Since the patches of diffuse reflecting surfaces have the same shape as the object surface itself, such classification provides relevant information to facilitate image analysis. For instance, a face, which resembles a convex sphere with small concavities, will be seen as a collection of intensity patches of concave functions ($\lambda_1 < 0$ and $\lambda_2 < 0$) for the forehead, the cheeks, the chin, and the nose and smaller patches of convex functions ($\lambda_1 > 0$ and $\lambda_2 > 0$) for the eyebrows, the eyes, the nostrils, and the mouth.

4 Results

In this section, we evaluate the proposed segmentation technique on the Berkeley segmentation dataset and benchmark (BSDS300).⁶³ The BSDS300 consists of 300 natural images, delivered with ground truth human annotations. To measure the difference between two segmentations, we examine the

PRI.⁶⁴ The PRI allows the comparison of a test segmentation algorithm using multiple ground truth images. It measures the fraction of pixel pairs, whose labels are consistent in the test segmentation and the ground truth one. The PRI averages over multiple ground truth segmentations and takes values in the interval, where 0 means that the acquired segmentation has no similarities with the ground truth and 1 means that the test and ground truth segmentations are identical.

To find the optimal parameter set of adaptive region growing, we measure the image approximation accuracy with a surface area weighted mean of the L_∞ fitting costs $\tilde{r}(S)$ of the polynomial surfaces. A high approximation accuracy (low mean fitting cost) gives a high number of smaller segments, providing a good approximation quality. On the other hand, a low approximation accuracy (high mean fitting cost) gives a low number of larger segments, providing approximation quality less well. Depending on the desired purpose (approximation or segmentation), one has to find a good balance between the size of the segments and the quality of the approximated images. Since the main purpose in this paper is rather segmentation, we set the segmentation parameters $T_X = 1.3$ and $T_Y = 2.8$. As we will show further on in the results, these parameters result in a maximum PRI.

Segmentation results on the BSDS300 are shown in Fig. 4. The columns (a)–(d) show the original gray-scale images, the segmented images, the reconstructed images, and the images with curvature indication, respectively. The PRIs are indicated below the images. The blue, green, and red colors in the images in column (b) correspond to zero, first, and second degree polynomial surfaces, respectively. We ascertain that many surface segments correspond to meaningful parts of the image. The polynomial surfaces in the images in column (c) provide good approximation of the image while preserving all the necessary details of the objects in the reconstructed images. In the images in column (d), the cyan, magenta, and yellow colors correspond to concave, convex, and saddle surfaces, respectively. For instance, in the face image, the head is a convex body part, seen as an intensity patch of a concave function.

Table 1 gives an overview of the mean and standard deviation of the computation time, the mean fitting cost, the number of surfaces and the PRI, respectively. Most of

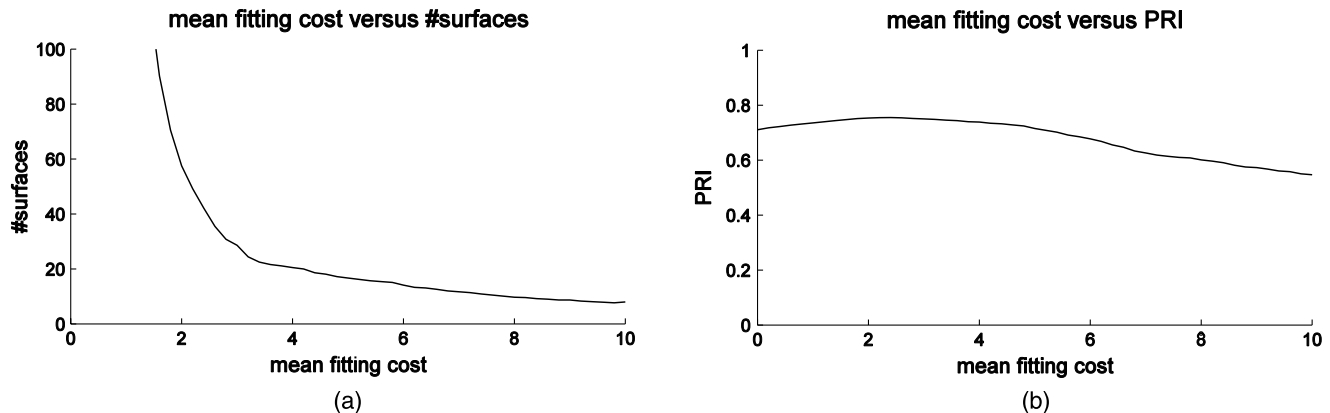


Fig. 6 The number of surface segments and the PRI versus the mean fitting cost: (a) This graph plots the numbers of surface segments when segmenting images of the BSDS300 for different mean fitting costs. For mean fitting costs of 3 or higher, the mean number of surface segments is relatively constant. For mean fitting costs of 3 or lower, the mean number of surface segments grows exponentially. (b) The graph in this figure plots the mean fitting cost versus the PRI. The PRI is maximal for a mean fitting cost of 2.5.

the computation time of the region-growing method is spent on the calculation of the fitting cost \tilde{r} . We developed a partially optimized program, which is implemented in C++ and running on a 2.8 GHz processor, 4 GB RAM, and 64-bit operating system. For images of size 240×160 , the computation time of our program is ~ 1.0 s/image. As a comparison, the computation time of the power watershed

algorithm²⁵ is ~ 1.2 s/image. When considering the number of surfaces, we find that our technique divides an image into only very few surface segments. The graph in Fig. 6(a) plots the numbers of surface segments when segmenting images of the BSDS300 for different mean fitting costs. We find that for mean fitting costs of 3 or higher, which corresponds to low approximation accuracies, the mean number of surface

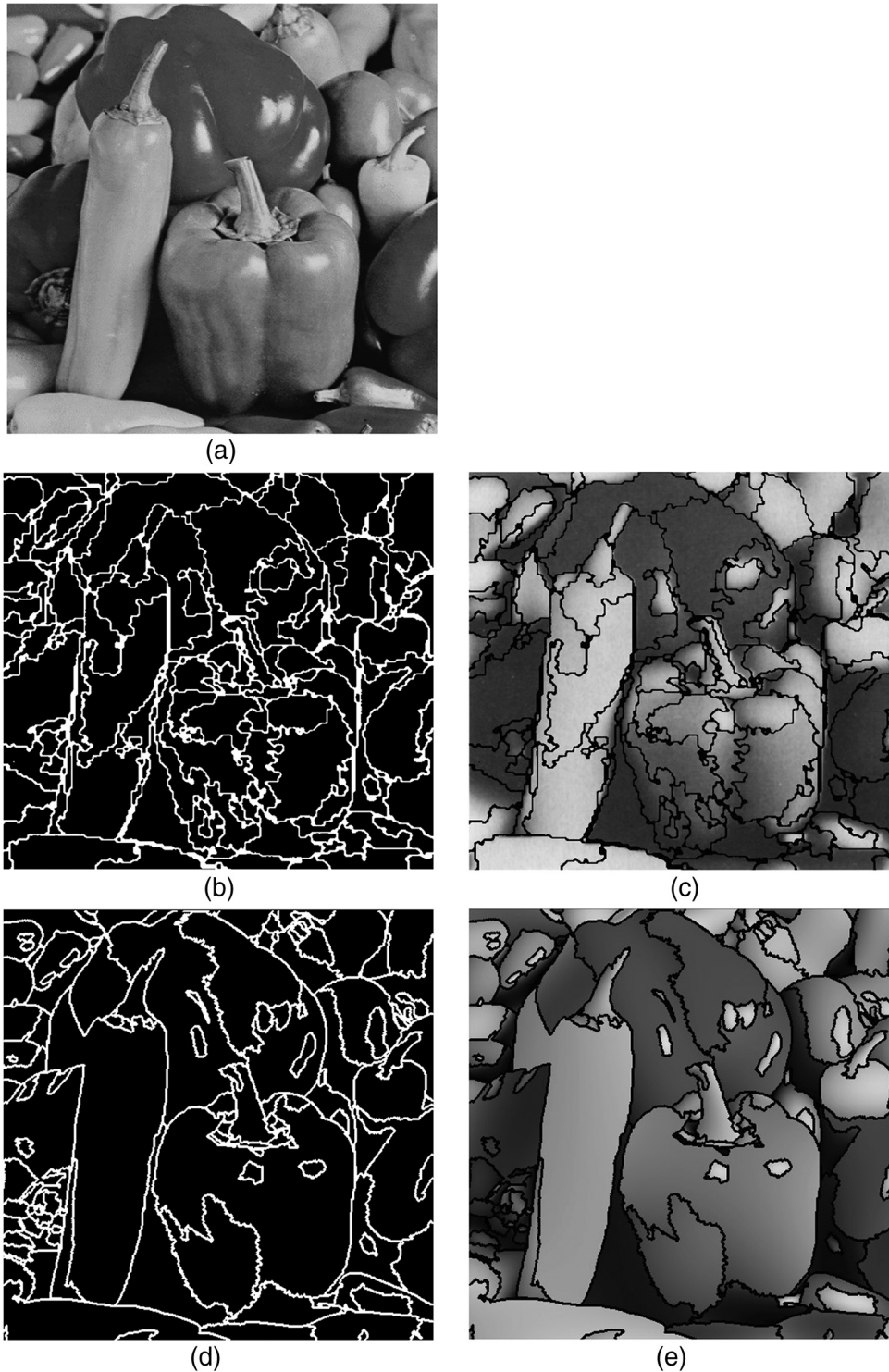


Fig. 7 Comparison with the polynomial segmentation technique proposed by Kocher and Leonardi et al. (Ref. 46) (a) The original gray-scale Peppers image with size 512×512 . (b, d) The segment boundaries produced by the method in Ref. 46 and our method, respectively. In both results, the number of segments is 129. Our method produces smoother segment boundaries. (c, e) The corresponding approximated images using quadratic surfaces. The root mean squared errors are both 15 gray levels on a 256 scale, respectively.

segments is relatively constant. This means that there is a small stable set of large segments. In contrast, for mean fitting costs of 3 or lower, which corresponds to high approximation accuracies, the mean number of surface segments grows exponentially. This means that there are many small segments.

We compare the proposed segmentation algorithm, which uses polynomial surfaces, with segments produced by normalized cuts,²³ mean shift,¹² and power watersheds.²⁵ To demonstrate the difference between the proposed method and existing techniques, we perform three tests. The first test is performed on all images of the BSDS300. The remaining two tests are performed on two subsets of images of the BSDS300. The first subset includes highly textured images, whereas the second subset contains images of objects with diffuse reflecting surfaces. Examples for both subsets are the desert image and the face image in Fig. 4, respectively. These subsets were carefully selected by computer vision experts.

A visual comparison of segmentation on a fish image with diffuse reflecting surfaces is shown in Fig. 5. Columns (b)–(e) on the second row show segmentations of image (a), produced by normalized cuts, mean shift, power watersheds, and polynomial surfaces, respectively. For these segmentation techniques, columns (f)–(i) on the third row show the segment approximations with polynomial surfaces of second degree as in Eq. (1). The power watershed algorithm uses the same seed pixels as produced by the proposed method. We can clearly ascertain that in contrast to the proposed method, the segments produced by existing segmentation techniques do not always coincide with object features and the contours separating the surface segments often do not correspond to real-image object edges. Furthermore, for existing techniques, the polynomial segment approximations do not accurately reconstruct the image.

An overview of the PRIs is given in Table 2. When testing the entire database, the segmentation results are comparable in terms of the PRI. As expected, the PRIs decrease when segmenting the more textured images of the first subset. For this subset, the proposed method performs less well when compared to the existing techniques. However, as for the desert image in Fig. 4, the segmentation result is visually still acceptable. Next, when segmenting images of the second subset, segmentation with polynomial surfaces significantly outperforms the existing techniques. This confirms that our method is primarily aimed at segmenting images into flat, planar, convex, concave, and saddle patches that correspond to meaningful parts of objects with diffuse reflecting surfaces. More comparing results on the BSDS300 in terms of the PRI are found in Ref. 68.

The graph in Fig. 6(b) plots the mean fitting cost versus the PRI for testing the entire database. We conclude that for a mean fitting cost of 2.5, the PRI is maximum. As mentioned in the beginning of this section, this maximum corresponds to the threshold parameters of adaptive region growing that are used in this paper.

As a last result, we compare our method with the polynomial segmentation technique proposed by Kocher and Leonardi.⁴⁶ Figure 7(a) presents the original gray-scale “Peppers” image with size 512×512 . Figures 7(b) and 7(d) illustrate the segment boundaries when applying the method in Ref. 46 and our method to the Peppers image, respectively. In both results, the number of segments is 129. We can

clearly observe that our method produces smoother segment boundaries than the method in Ref. 46. Smooth segment boundaries facilitate the task of object recognition. Figures 7(c) and 7(e) exhibit the corresponding approximated images using quadratic surfaces. The root mean squared errors are both 15 gray levels on a 256 scale, respectively.

5 Conclusion

In this work, image segmentation is performed on gray-scale images by adaptive region growing based on low-degree polynomial fitting. This novel algorithm uses the adaptive thresholding of the L_∞ fitting cost to detect outliers and edges, distinguishes between strong and smooth intensity transitions, and interprets gray levels using a geometric point of view approach. Images are represented by flat, planar, convex, concave, and saddle polynomial surfaces with a variable fitting error. The proposed method performs well in segmenting images into patches that correspond to meaningful parts of objects with diffuse reflecting surfaces. In contrast to existing segmentation techniques, the segments produced by the proposed method correspond more to object features, the contours separating the surface segments coincide with real-image object edges, and the low-degree polynomial approximations accurately reconstruct the image. However, the method performs less well in segmenting images of objects with highly textured patterns. For object recognition purposes, curvature-based classification of surface segments provides important shape information of the image objects.

Acknowledgments

The work was financially supported by iMinds and IWT through the project “iCoCoon” and by FWO through the project G.0.398.11.N.10 “Multi-camera human behavior monitoring and unusual event detection.”

References

1. S. K. Shah, “Performance modeling and algorithm characterization for robust image segmentation,” *Int. J. Comput. Vision* **80**(1), 92–103 (2008).
2. J. H. Lambert, *Photometria Sive de Mensura de Gratibus Luminis, Colorum et Umbrae*, Eberhard Klett, Augsburg, Germany (1760).
3. J. Wagemans, A. J. Van Doorn, and J. Koenderink, “The shading cue in context,” *i-Perception* **1**(3), 159–177 (2010).
4. K. S. Fu and J. K. Mui, “A survey on image segmentation,” *Pattern Recognit.* **13**(1), 3–16 (1981).
5. R. Haralick and L. G. Shapiro, “Survey: image segmentation techniques,” *Comput. Vision Graphics Image Process.* **29**(1), 100–132 (1985).
6. R. Nevatia, “Image segmentation,” in *Handbook of Pattern Recognition, and Image Processing*, T. Y. Young and K. S. Fu, Eds., Vol. 86, pp. 215–231, Academic Press, Orlando (1986).
7. N. R. Pal and S. K. Pal, “A review of image segmentation techniques,” *Pattern Recognit.* **26**(9), 1277–1294 (1993).
8. X. Muñoz et al., “Strategies for image segmentation combining region and boundary information,” *Pattern Recognit. Lett.* **24**(1–3), 375–392 (2003).
9. N. Otsu, “A threshold selection method from grey-level histograms,” *IEEE Trans. Systems Man Cybernet.* **9**(1), 62–66 (1979).
10. J. N. Kapur, P. K. Sahoo, and A. K. C. Wong, “A new method for gray-level picture thresholding using the entropy of the histogram,” *Comput. Vision Graphics Image Process.* **29**(3), 273–285 (1985).
11. Y. Deng and B. S. Manjunath, “Unsupervised segmentation of color-texture regions in images and video,” *IEEE Trans. Pattern Anal. Mach. Intell.* **23**(8), 800–810 (2001).
12. D. Comaniciu and P. Meer, “Mean shift: a robust approach toward feature space analysis,” *IEEE Trans. Pattern Anal. Mach. Intell.* **24**(5), 603–619 (2002).
13. J. Chen et al., “Adaptive perceptual color-texture image segmentation,” *IEEE Trans. Image Process.* **14**(10), 1524–1536 (2005).

14. J. F. Aujol and T. F. Chan, "Combining geometrical and textured information to perform image classification," *J. Visual Commun. Image Represent.* **17**(5), 1004–1023 (2006).
15. W. Tao, H. Jin, and Y. Zhang, "Color image segmentation based on mean shift and normalized cuts," *IEEE Trans. Syst. Man Cybernet.* **37**(5), 1382–1389 (2007).
16. M. Mignotte, "Segmentation by fusion of histogram-based k-means clusters in different color spaces," *IEEE Trans. Image Process.* **17**(5), 780–787 (2008).
17. L. Vincent and P. Soille, "Watersheds in digital spaces: an efficient algorithm based on immersion simulations," *IEEE Trans. Pattern Anal. Mach. Intell.* **13**(6), 583–598 (1991).
18. F. Y. Shih and S. Cheng, "Automatic seeded region growing for color image segmentation," *Image Vision Comput.* **23**(10), 877–886 (2005).
19. S. Makrogiannis, G. Economou, and S. Fotopoulos, "A region dissimilarity relation that combines feature-space and spatial information for color image segmentation," *IEEE Trans. Syst. Man Cybernet. B* **35**(1), 44–53 (2005).
20. A. Y. Yang et al., "Unsupervised segmentation of natural images via lossy data compression," *Comput. Vision Image Underst.* **110**(2), 212–225 (2008).
21. Y. Tarabalka, J. Chanussot, and J. A. Benediktsson, "Segmentation and classification of hyperspectral images using watershed transformation," *Pattern Recognit.* **43**(7), 2367–2379 (2010).
22. Z. Liu, L. Shen, and Z. Zhang, "Unsupervised image segmentation based on analysis of binary partition tree for salient object extraction," *Signal Process.* **91**(2), 290–299 (2011).
23. J. Shi and J. Malik, "Normalized cuts and image segmentation," *IEEE Trans. Pattern Anal. Mach. Intell.* **22**(8), 888–905 (2000).
24. S. Wang and J. M. Siskind, "Image segmentation with ratio cut," *IEEE Trans. Pattern Anal. Mach. Intell.* **25**(6), 675–690 (2003).
25. C. Couprie et al., "Power watershed: a unifying graph-based optimization framework," *IEEE Trans. Pattern Anal. Mach. Intell.* **33**(7), 1384–1399 (2011).
26. M. Eden and M. Kocher, "On the performance of a contour coding algorithm in the context of image coding part 1: contour segment coding," *Signal Process.* **8**(4), 381–386 (1985).
27. M. Kunt, M. Benard, and R. Leonardi, "Recent results in high-compression image coding," *IEEE Trans. Circuits Syst.* **34**(11), 1306–1336 (1987).
28. M. Gilge, T. Engelhardt, and R. Mehlan, "Coding of arbitrarily shaped image segments based on a generalized orthogonal transform," *Signal Process. Image Commun.* **1**(2), 153–180 (1989).
29. W. Philips, "Fast coding of arbitrarily shaped image segments using weakly separable bases," *Opt. Eng.* **35**(1), 177–186 (1996).
30. C. A. Christopoulos et al., "Segmented image coding: techniques and experimental results," *Signal Process. Image Commun.* **11**(1), 63–80 (1997).
31. M. M. Reid, R. J. Millar, and N. D. Black, "Second-generation image coding: an overview," *ACM Comput. Surv.* **29**(1), 3–29 (1997).
32. S. Biswas, "Segmentation based compression for graylevel images," *Pattern Recognit.* **36**(7), 1501–1517 (2003).
33. A. A. Kassim, W. S. Lee, and D. Zonoobi, "Hierarchical segmentation-based image coding using hybrid quad-binary trees," *IEEE Trans. Image Process.* **18**(6), 1284–1291 (2009).
34. S.-H. Cha, "Comprehensive survey on distance/similarity measures between probability density functions," *Int. J. Math. Models Methods Appl. Sci.* **1**(4), 300–307 (2007).
35. T.-J. Fan, G. Medioni, and R. Nevatia, "Recognizing 3-D objects using surface descriptions," *IEEE Trans. Pattern Anal. Mach. Intell.* **11**(11), 1140–1157 (1989).
36. Y. S. Lim, T. I. Cho, and K. H. Park, "Range image segmentation based on 2D quadratic function approximation," *Pattern Recognit. Lett.* **11**(10), 699–708 (1990).
37. G. Taubin, "Estimation of planar curves, surfaces, and nonplanar space curves defined by implicit equations with applications to edge and range image segmentation," *IEEE Trans. Pattern Anal. Mach. Intell.* **13**(11), 1115–1138 (1991).
38. L. Wang, J. Cao, and C. Han, "Multidimensional particle swarm optimization-based unsupervised planar segmentation algorithm of unorganized point clouds," *Pattern Recognit.* **45**(11), 4034–4043 (2012).
39. T. Rabbani, F. A. van den Heuvel, and G. Vosselman, "Segmentation of point clouds using smoothness constraint," in *Proc. International Archives of Photogrammetry, Remote Sensing and Spatial Information Sciences*, Dresden, Germany, Vol. 36, pp. 248–253 (2006).
40. J. E. Deschaud and F. Goulette, "A fast and accurate plane detection algorithm for large noisy point clouds using filtered normals and voxel growing," in *Proc. Fifth Int. Symp. 3D Data Processing, Visualization and Transmission*, Paris, France, pp. 248–253 (2010).
41. P. J. Besl and R. C. Jain, "Segmentation through variable-order surface fitting," *IEEE Trans. Pattern Anal. Mach. Intell.* **10**(2), 167–192 (1988).
42. M. Vieira and K. Shimada, "Surface mesh segmentation and smooth surface extraction through region growing," *Comput. Aided Geometric Des.* **22**(8), 771–792 (2005).
43. G. Lavoué, F. Dupont, and A. Baskurt, "A new CAD mesh segmentation method, based on curvature tensor analysis," *Comput. Aided Des.* **37**(10), 975–987 (2005).
44. A. Jagannathan and E. L. Miller, "Three-dimensional surface mesh segmentation using curvedness-based region growing approach," *IEEE Trans. Pattern Anal. Mach. Intell.* **29**(12), 2195–2204 (2007).
45. J. Wang and Z. Yu, "Geometric decomposition of 3D surface meshes using Morse theory and region growing," *Int. J. Adv. Manuf. Technol.* **56**(9–12), 1091–1103 (2011).
46. M. Kocher and R. Leonardi, "Adaptive region growing technique using polynomial functions for image approximation," *Signal Process.* **11**(1), 47–60 (1986).
47. G. Wang et al., "An estimation-based approach for range image segmentation: on the reliability of primitive extraction," *Pattern Recognit.* **36**(1), 157–169 (2003).
48. D. Cohen-Steiner, P. Alliez, and M. Desbrun, "Variational shape approximation," *ACM Trans. on Graphics (SIGGRAPH)* **23**(3), 905–914 (2004).
49. W. Wang, "Modelling and processing with quadric surfaces," in *Handbook of Computer Aided Geometric Design*, G. Farin, J. Hoschek, and M. S. Kim, Eds., pp. 777–795, Elsevier, North-Holland (2002).
50. S. Petitjean, "A survey of methods for recovering quadrics in triangle meshes," *ACM Comput. Surv.* **34**(2), 211–262 (2002).
51. D.-M. Yan et al., "Variational mesh segmentation via quadric surface fitting," *Computer-Aided Des.* **44**(11), 1072–1082 (2012).
52. J. Wu and L. Kobbelt, "Structure recovery via hybrid variational surface approximation," *Comput. Graphics Forum (EUROGRAPHICS)* **24**(3), 277–284 (2005).
53. P. Simari and K. Singh, "Extraction and remeshing of ellipsoidal representations from mesh data," in *Proc. Graphics Interface*, pp. 161–168, Canadian Human-Computer Communications Society School of Computer Science, University of Waterloo, Waterloo, Ontario, Canada (2005).
54. S. Zucker, "Region growing: childhood and adolescence," *Comput. Graphics Image Process.* **5**(3), 382–399 (1976).
55. R. Adams and L. Bischof, "Seeded region growing," *IEEE Trans. Pattern Anal. Mach. Intell.* **16**(6), 641–647 (1994).
56. C.-C. Kanga, W.-J. Wang, and C.-H. Kang, "Image segmentation with complicated background by using seeded region growing," *Int. J. Electron. Commun.* **66**(9), 767–771 (2012).
57. R. Pohle and K. D. Toennies, "Segmentation of medical images using adaptive region growing," *Proc. SPIE* **4322**, 1337 (2001).
58. A. K. Qin and D. A. Clausi, "Multivariate image segmentation using semantic region growing with adaptive edge penalty," *IEEE Trans. Image Process.* **19**(8), 2157–2170 (2010).
59. P. Veelaert, "Constructive fitting and extraction of geometric primitives," *CVGIP Graph. Models Image Process.* **59**(4), 233–251 (1997).
60. P. Veelaert and K. Teelen, "Fast polynomial segmentation of digitized curves," in *Proc. of Discrete Geometry for Computer Imagery*, pp. 482–493, LNCS, Springer-Verlag, Berlin, Heidelberg (2006).
61. K. Sim and R. Hartley, "Removing outliers using the L_∞ norm," in *Proc. of Computer Vision and Pattern Recognition*, pp. 485–494, IEEE (2006).
62. F. Deboeverie et al., "Adaptive constructive polynomial fitting," in *Proc. of Advanced Concepts for Intelligent Vision Systems*, pp. 173–184, LNCS, Springer-Verlag, Berlin, Heidelberg (2010).
63. D. Martin et al., "A database of human segmented natural images and its application to evaluating segmentation algorithms and measuring ecological statistics," in *Proc. of IEEE Int. Conf. on Computer Vision*, Vol. 2, pp. 416–423, IEEE (2001).
64. C. Pantofaru and M. Hebert, "A Comparison of Image Segmentation Algorithms," Technical Report, No. CMU-RI-TR-05-40, Robotics Inst., Carnegie Mellon Univ. (2005).
65. J. Yuan, D. L. Wang, and R. Li, "Image segmentation using local spectral histograms and linear regression," *Pattern Recognit. Lett.* **33**(5), 615–622 (2012).
66. M. Mignotte, "A de-texturing and spatially constrained K-means approach for image segmentation," *Pattern Recognit. Lett.* **32**(2), 359–367 (2011).
67. R. Huang et al., "Image segmentation via coherent clustering in L.a.b. color space," *Pattern Recognit. Lett.* **32**(7), 891–902 (2011).
68. P. Arbeláez et al., "Contour detection and hierarchical image segmentation," *IEEE Trans. Pattern Anal. Mach. Intell.* **33**(5), 898–916 (2011).
69. P. Veelaert, Separability and tight enclosure of point sets, in *Digital Geometry Algorithms, Theoretical Foundations and Applications to Computational Imaging*, V. E. Brimkov and R. P. Barneva, Eds., Vol. 2, pp. 215–243, Lecture Notes in Computational Vision and Biomechanics, Springer Science+Business Media, Dordrecht (2012).



image interpretation with polynomial feature models for real-time vision systems.

Francis Deboeverie received his Master of Science in electronics and ICT engineering technology from the University of Ghent in Belgium in 2007. After his studies, he joined the department of telecommunications and information processing of Ghent University, where he currently does research on image processing problems. He is currently a PhD candidate at the image processing and interpretation group (IPI-TELIN-iMinds) at Ghent University. His research interests include

sciences, Ghent University. His current research interests include real-time systems for low-level vision, image interpretation of road scenes, and geometric uncertainty models.



Wilfried Philips received his diploma degree in electrical engineering in 1989 and his PhD degree in applied sciences in 1993, both from Ghent University, Belgium. From 1989 until 1997, he worked at the Department of Electronics and Information Systems of Ghent University for the Flemish Fund for Scientific Research (FWO-Vlaanderen), first as a research assistant and later as a post-doctoral research fellow. Since November 1997, he is with the department of telecom-

munications and information processing of Ghent University, where he is currently a full-time professor and is heading the research group Image Processing and Interpretation, which is also a part of the Flemish ICT research institute iMinds. Some of the recent research activities in the group include image and video restoration and analysis, image and video quality assessment and image analysis and computer vision. Important application areas targeted by the group include surveillance, industrial inspection, and HD video improvement.



Peter Veelaert received his degree in electronic engineering from the University of Ghent in 1981. After his studies, he started working as an engineer at the Digitized Information Systems Corporation, Belgium, where he developed computer graphics software. In 1986, he joined the Laboratory for Electronics at the University of Ghent from where he received a PhD degree in 1992. He currently teaches and does research at the department of applied engineering